Applications in Energy and Combustion Science 20 (2024) 100294

Contents lists available at ScienceDirect

Applications in Energy and Combustion Science

journal homepage: www.elsevier.com/locate/jaecs

Experimental investigation of irradiance from combustion in porous media with different geometries

Petra Weinbrecht *, Björn Stelzner, Peter Habisreuther, Christof Weis, Dimosthenis Trimis

Karlsruhe Institute of Technology, Engler-Bunte-Institute Combustion Technology, Engler-Bunte-Ring 7, 76131 Karlsruhe, Germany

ARTICLE INFO

Keywords:
Radiant porous burner
Radiation efficiency
Kelvin cell
Premixed combustion
Additive manufacturing
Computer tomography
Specific surface area
Hendecahedron

ABSTRACT

Radiant porous burners with a high power density, emitting intense radiation were investigated. Different geometrical structures were applied as porous inlay in a state-of-the-art, two-layer porous burner with a rectangular shape. Structures were made of SiSiC and manufactured by the replica method using foaming and hybrid additive manufacturing. Subject to the study were foam structures as well as lattice structures with random strut distribution based on the Voronoi tessellation and with regular distribution based on the Kelvin and Hendecahedron cell geometry. The structures were designed with the intention of enhancing the irradiation by optimising the specific surface area distribution along the flow direction. The additive manufacturing method enables this through a local increase in pore density and the implementation of additional surfaces. Image processing was used to demonstrate the effectiveness of this approach and to characterise the structures in specific surface areas. Volume averaged values and distribution along the thickness were analysed. The radiation efficiency was derived from measurements of the radiation intensity on discrete points in parallel to the radiating surface using a radiometer. The burner was operated with methane as fuel at a specific burner power in the range of $600\,\mathrm{kW\,m^{-2}}$ to $1000\,\mathrm{kW\,m^{-2}}$ and an equivalence ratio of $\phi = 0.7$. Measured radiation efficiency was compared to a limiting radiation efficiency obtained from theoretical calculations. Highest radiation efficiency was obtained for a foam structure with a specific surface area of $622\,\mathrm{m^{-1}}$. Structures based on the geometry of a hendecahedron and a kelvin cell achieved comparable efficiencies. The lowest values were observed for a randomly distributed lattice structure with nominal pore density of 10 PPI. A relation between volume averaged specific surface area values and measured radiation efficiency is derived and proven. Additionally, efficiency could be improved by targeted surface area increase applying closed windows or a gradient in pore size respectively.

Contents

1. Introduction 2
2. Material and methods 3
   2.1. Porous radiant burner 3
   2.2. Porous ceramic structures 3
   2.3. Determination of mean and local specific surface area 4
      2.3.1. Specific surface area of manufactured structures 4
      2.3.2. Specific surface determination of 3D-models 5
   2.4. Experimental methods 6
      2.4.1. Test rig 6
      2.4.2. Procedure 6
3. Theory 7
4. Results and discussion 8
   4.1. Specific surface area 8
      4.1.1. Comparison of 3D-model and CT-scan 9
   4.2. Radiation efficiency 10
   4.3. Relation between S_V and η_{rad} 11

* Corresponding author.
E-mail address: petra.weinbrecht@partner.kit.edu (P. Weinbrecht).

https://doi.org/10.1016/j.jaecs.2024.100294
Received 19 May 2024; Received in revised form 12 September 2024; Accepted 24 September 2024
Available online 9 October 2024
2666-352X/© 2024 The Authors. Published by Elsevier Ltd. This is an open access article under the CC BY-NC license (http://creativecommons.org/licenses/by-nc/4.0/).

5. Conclusions 11
CRediT authorship contribution statement 11
Declaration of competing interest 11
Data availability 12
Acknowledgements 12
References 12

1. Introduction

Radiant porous burners (RPBs) are characterised by premixed flame stabilisation in a porous media with modest dimension in flow direction resulting in high solid temperatures with low pollutant emissions [1–3]. In particular, radiant burners with a two-layer design [4] are characterised by the emission of intense thermal radiation exceeding high area specific thermal power up to $2000\,\mathrm{kW\,m^{-2}}$ [5]. This burner design incorporates a flame trap to prevent the flame from upstream propagation [6]. The flame stabilises within the open pore ceramic structure reaching a stationary equilibrium between conductive, convective and radiative heat transfer. Heat recirculation in the solid phase and dispersion within the fluid phase result in an increased thermal flame thickness and effective flame speed compared to the freely burning laminar flame [7–9]. The thermal inertia of the solid expands the stability limits, allowing operation in wide power and equivalence ratio ranges and the application of low calorific value gases [10,11]. The porous structure, not contributing to the chemical reaction is often termed as porous inert medium (PIM) [6] and can be made of rather packed beds [12–17], porous ceramic structures [18–21] or porous metallic structures, printed [22] or sintered [23]. Due to its remarkable mechanical and chemical stability in high temperature oxidative environments, ceramic materials such as silicon carbide (SiC) have proven to be suitable for the use in RPB [24,25]. In addition, the oxidation and thermal shock resistance of the material can be further enhanced by silicon infiltration, resulting in SiSiC [26,27]. Porous SiSiC is often produced in foam like structures with a random distribution of cells and lattices using the replica method [26,28]. Recent developments enable the additive manufacturing of the polymer template as geometrically defined lattice structures, which can also be processed by the replica method [29,30]. Ceramics based on this hybrid additive manufacturing method can be applied in RPBs [31]. According to experimental investigations [32–35], those structures exhibit enhanced durability and comparable combustion properties when compared to ceramic foams. Furthermore, the improved repeatability of pore size and density is advantageous in influencing burner performance [36]. The hybrid manufacturing method allows for the production of ceramic lattice structures with specific properties, such as strut size and distribution [29], which can be tailored to suit the intended application. The implementation of these structures in RPBs has the potential to enhance radiation efficiency, which is of particular significance in energy-intensive manufacturing industries that rely on advanced radiant heat transfer. This, in turn, has a direct impact on the energy consumption of the process [37]. RPBs based on the design evaluated in the present study are characterised by a flame stabilisation near the interface between flame trap and the combustion zone [38]. High temperatures are expected to be reached in this region and can be enhanced by providing surface area for the convective heat transfer. The physical principles of radiant heat transfer state that an increase in radiant heat output can be achieved by increasing the surface area and solid temperature of the radiating body. As open-cell structures are to be treated as volumetric radiation emitters, and due to the complexity of the heat transfer processes involving recirculating and emitting heat flows within the structure, a straight-forward prediction of the impact of changes in the geometrical properties of the structures on the radiation output is not possible. Furthermore, experimental investigations of radiant output from lattice structures implemented in RPBs for the application in manufacturing industries have not been reported in the literature to date. The objective of this study is to close this gap and to determine the influence of the geometrical structure of the ceramic inlay of a RPB manufactured by hybrid manufacturing with a standardised and radiation output enhanced design on the radiation efficiency. The performance of these structures is evaluated in comparison to foam structures, which are employed as a reference.

Measurements of radiation output of RPB from literature are based on various measurement techniques. Radiation intensity can be measured using a radiometer equipped with a pyroelectric sensor. In 1995, Speyer et al. [39] studied the radiation output of a variety of burners radiating perpendicular to the ground using a fixed position total radiation pyrometer. Later, Caetano et al. used a similar configuration to evaluate SiC and zirconium ceramics with different pore densities [20]. Mital et al. [40] further developed this technique by measuring the distribution of the incident heat flux on the surface of an imaginary semi-infinite cylinder enclosing the burner to measure the radiation output of a cordierite structure radiating in the upward direction. In a later publication [41], Mital presented a technique for measuring highly directional radiating burners using a multi-point measurement in a horizontal orientation parallel to the burner surface.

Abdelaal et al. (2013) employed identical equipment and configuration to assess the radiation efficiency of a Mullite structure with an 85% porosity, operated with natural gas over a wide range of equivalence ratios and specific powers [42]. In another study, Maznoy et al. [23] used a pyrometer rotating around the centre axis of the burner measuring the local heat flux to investigate the radiative efficiency of a cylindrical Ni–Al alloy emitter with different pore densities. Another possibility to determine the solid surface radiation is the surface temperature measurement with a infrared thermography camera either mounting the burner perpendicular to the floor [43], radiating upwards and applying reflecting optics [18], or positioning the measurement device at an angle [44]. Mital et al. [41] also proposed a calorimetric heat transfer measurement technology, that uses a cooled plate with high emissivity for radiative and convective heat flux measurement and a plate with high reflectivity for convective heat flux measurement. The results demonstrate radiation efficiencies that align well with pyrometer measurements.

Numerical studies of the radiative efficiency of a porous radiant burner comparable to that investigated by Maznoy et al. have been carried out by Vahidhosseini et al. [45]. Investigations of two-layer porous burners range from pore-resolved calculations of foam structures [9] and lattice structures [46] to reduced one-dimensional models [47], which are advantageous due to the lower computational effort. Moreover, Wieland et al. [46] examined a comparable configuration in their study, specifically examining the impact of structural geometry on radiation output.

Overall, studies on RPBs have mainly focused on the effect of the equivalence ratio and the specific power on the emission of pollutants and the surface temperature of RPBs with foam-like structures, e.g. [43,48]. These studies only provide a brief assessment of the impact of characteristic parameters, such as pore density and specific surface, on combustion and radiation properties [20]. In studies where specific surface area values are provided in the research field of radiation efficiency of RPBs, these are determined by correlations based on mathematical or empirical analyses. Given the variability of methods in the manufacturing processes such correlations are not reliable [49].

The present study addresses this gap by providing the specific surface area of the investigated structures as a traceable geometrical

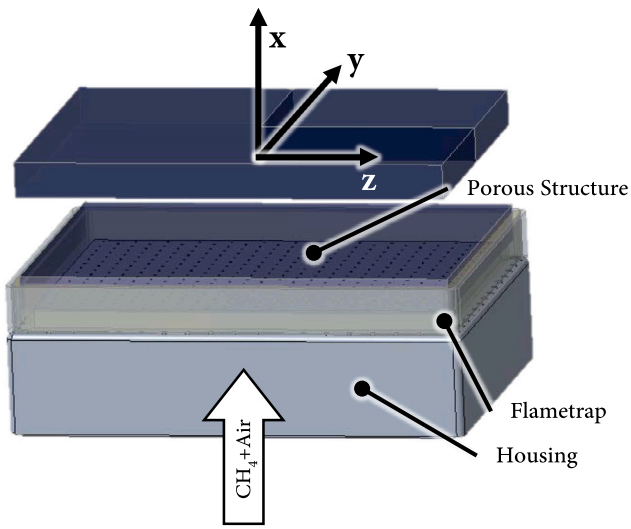

Fig. 1. Porous burner assembly sketch with coordinate definition.

property derived from computed tomography scans. In addition, a comparison between the preliminary design model and the finished structure in terms of the mean and local specific surface area is used to assess the correspondence between the originally conceived design and its actual realisation. For the determination of the radiated power a standardised measurement technique for the determination of the radiated total power of gas-fired overhead luminous radiant heaters has been adapted for use with high power density burners, thereby ensuring the reproducibility of the results. The radiation efficiency is evaluated in accordance with a theoretical limit value derived from thermodynamic equilibrium.

2. Material and methods

The determination of the radiation efficiency of different structures is based on the determination of the radiant flux. The relationship between geometrical parameters and radiation efficiency of structures is a main objective of the present work. This section includes the introduction of the burner, the studied structures, the procedure of data processing of 3D computed tomography scans to derive geometrical parameters, the test rig and the experimental procedure to determine the radiant flux.

2.1. Porous radiant burner

The radiant porous burner under investigation is designed to be operated with pre-mixed natural gas – air in a lean condition. The mixer consist of a tube with an inner diameter of 20 mm in which fuel is injected via a nozzle with an inner diameter of 0.5 mm in a jet in co-flow configuration [50]. The mixture passes through a flow obstacle in the form of a perforated plate, which supports an even flow distribution in the cross-section of the burner manifold and subsequent flame trap. The flame trap is 20 mm thick and is made mainly of aluminium oxide with a rectangular hole pattern each 1 ± 0.15 mm in diameter. The flame stabilises downstream of the flame trap inside the porous ceramic structure of 185 mm x 136 mm cross sectional extend.

The structure has a nominal thickness of 15 mm or 20 mm fixed in position by a metal housing and an expanding soft gasket (DuoSeal, DuothermStark GmbH). This gasket fastens the structure, minimises air entrainment in the combustion zone and acts as insulation. A schematic overview of the burner assembly and the coordinate system is shown in Fig. 1.

2.2. Porous ceramic structures

Seven structures are subject to this study. These can be classified in regular or random lattice and random foam structures. The structures are made of silicon infiltrated silicon carbide (SiSiC) and were produced via the replica method by EngiCer SA (Switzerland). Similar structures have been used in previous works [48,51,52]. This material exhibits excellent radiation properties with an $\varepsilon = 0.9$ [53] and high thermal shock resistance. Furthermore, it is capable of being applied at a high maximum temperature of 1723 K [54,55] before Si melting and oxidation of the material weakens structural stability and leads to destruction [56,57]. Literature provides no evidence that SiC has a catalytic effect on gases containing hydrocarbons. Furthermore, the probability of a collision between a gas molecule and the solid is significantly lower than a collision between gas molecules. It follows that a possible reaction between gas and solid would have a significantly lower impact on the combustion than the gas reaction. Therefore, the solid can be considered inert.

Random foam structures and lattice structures differ in the initial stages of the production, the manufacturing of the polymer template. Templates can be produced by foaming a suspension of polymers to generate random foams or by using additive manufacturing methods [29] to create defined lattice structures. As outlined in [58], hollow strut networks constitute the final product after following all the manufacturing procedures.

Hybrid additive manufacturing [29] presents many design possibilities. One potential design is based on basic networks formed from unit cells that can be seamlessly repeated in various spatial directions to achieve the desired plate size. This study examined two types of such unit cell networks. The Kelvin cell, also known as a tetrakaidecahedron with 14 faces, is an approximation of a close packing of equal spheres and is commonly utilised as a model for regular monodisperse foams [31,59,60]. Consequently, this structure is subjected to numerical [46] and experimental studies with the objective of evaluating the impact of open cell and strut size on combustion and radiation performance [61]. In this study, a unit cell network is created using the edge lines of the faces and scaled to achieve a structure size of approximately 20 mm in the x-direction (see Fig. 1) with three stacked unit cells. One unit cell is proportionally adjusted to fully enclose a sphere having an equal inner diameter of 5 mm with a strut width of 1.1 mm. This unit cell was subsequently repeated in both the y- and z-directions to form the studied kelvin cell structure. In this study, the structure is modified with respect to its local specific surface area and for improved performance in RPB concerning radiation efficiency. This is achieved by closing the pore openings [62], also called windows, as adapted from Habisreuther et al. [63] proven to increase residence time and flow tortuosity in porous structures. Here, the windows in the first two of the three unit cells were closed reciprocally in order to provide a larger surface area for convective heat transfer and to simultaneously prevent the obstruction of radiation paths to the environment. The modification is represented by opaque areas within the strut network, as illustrated in Fig. 2 (b). Another investigated structure, the bi-symmetric hendecahedron consists of 11 faces and is also a space-filling polyhedron [64], which can be used to generate a tessellation of space [65]. The structure shown in Fig. 2 (c) is created by stacking and shifting hendecahedron, resulting in junctions composed of up to six struts. The unit cell was scaled to realise a distance from the junction of four struts to the rhomboid plane of 5 mm. Due to the high number of junctions per volume at comparable cell and strut diameter of 1.1 mm, the generated structure promises a larger specific surface area than KC and therefore higher radiated power.

3D-printable models representing the variability and irregularity of open-cell foams are investigated with another design based on Voronoi tessellation. As demonstrated in [66], this involves dividing space using randomised seed points to generate structures with pore sizes that either mimic the current random foam state or incorporate

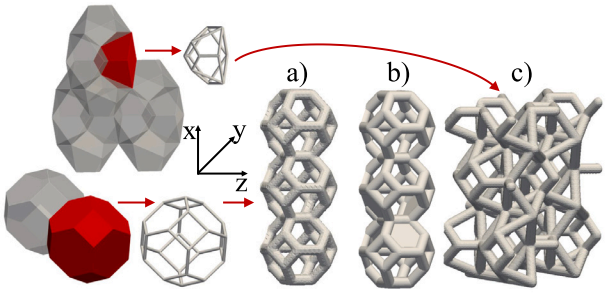

Fig. 2. Illustration of space filling unit cells structures and the formation of strut networks to the (a) kelvin cell structure (KC) (b) optimised kelvin cell structure (opt. KC) and the (c) hendecahedron structure (HK).

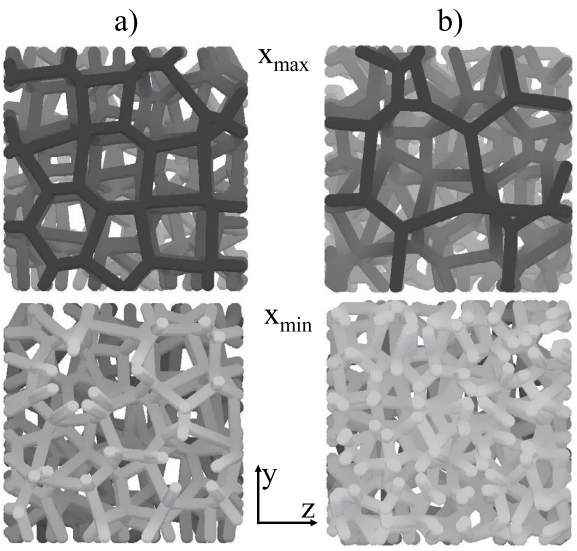

Fig. 3. Illustration of the lower side (x_{min}) and upper side (x_{max}) of the 3D Model of the investigated Voronoi structure (Voro) (a) without gradient in pore size and (b) with gradient in pore size (VwG) coloured from light grey to dark grey according to x-coordinate.

a pore size gradient. A Voronoi structure with continuous graded pore densities in the range from 10 PPI to 3 PPI in the flow direction was generated to investigate the effect of a defined variation in pore size in random structures as illustrated in Fig. 3 (b). As with the optimised KC structure, this configuration should facilitate a larger surface area for convective heat transfer in the region of the flame stabilisation area, while simultaneously preventing the obstruction of radiation paths to the surrounding environment by the presence of pores with large diameters at the exit of the porous inlay. In order to facilitate a comparison between the random foams and the additively manufactured lattice structures, which are characterised by triangular or circular struts respectively, a further structure was investigated. A voronoi structure without gradient and a verified pore density of 6 PPI represents this structure and is illustrated in Fig. 3 (a).

Random foams produced by foaming of the polymeric suspension were supplied with a pore density of 10 PPI according to the manufacturer's specifications and a total extent of 19.69 ± 0.21 mm and 15.43 ± 0.15 mm, visualised in Fig. 4 (a) and (b) respectively. Strut counting on a set path length on the structures surface revealed a true pore density of 9±1 PPI and 6±1 PPI for RF20 and RF15 respectively. This results in larger pores for RF15, as can also be seen in Fig. 4 (a) compared to (b). Due to the randomness in the manufacturing process, the actual thickness for KC, opt. KC, HK and the Voronoi structure results in 20.86 mm to 21.12 mm with an uncertainty of ±0.15 mm, summarised in Table 1. The porosity defined by $\Psi = 1 - (m \cdot V_{total}{}^{-}1 \cdot \rho_{SiSiC}{}^{-}1) \cdot$

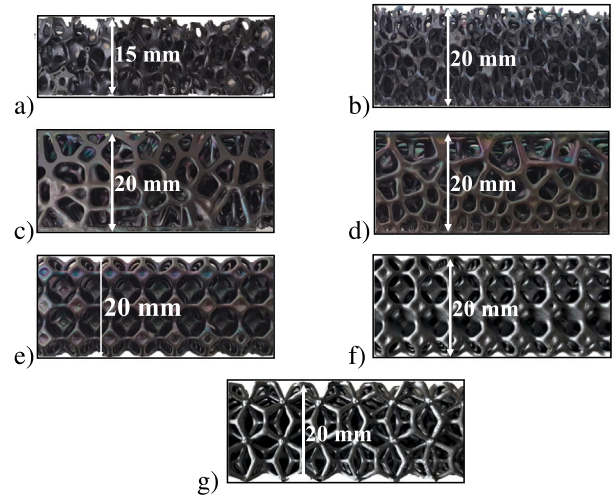

Fig. 4. Picture of side view in x–z-plane of samples (a) Random foam 15 mm (RF15), (b) Random foam 20 mm (RF20), (c) Voronoi (Voro), (d) Voronoi with gradient (VwG), (e) Kelvin cell (KC), (f) Optimised kelvin cell (opt. KC) and (g) Hendecahedron (HK).

100 % can be calculated from the weighed mass m and the density of $\rho_{SiSiC} = 2380\,\mathrm{kg\,m^{-3}}$ [29]. The total volume V_{total} is calculated from the measured thickness and the dimensions in the y- and z-directions of 136.5±0.17 and 185.5±0.27. For the investigated samples the porosity ranges from 82 % to 85 % with the lowest value for opt. KC and highest for the foam and KC structure.

2.3. Determination of mean and local specific surface area

Information on the surface area of porous structures with a large extension and a high porosity can be obtained by means of imaging techniques [67]. The specific surface area is the ratio between surface area and volume of the structure. It can be also derived from 3D models applied for template generation in the manufacturing process. In the following sections, procedures for determining specific surface area from CT scans of manufactured samples and subsequently from 3D models generated for hybrid additive manufacturing are explained.

2.3.1. Specific surface area of manufactured structures

Structures were scanned with a computer tomograph (Metronome 800, 225 kV HR, Zeiss GmbH) at a X-ray tube voltage of 190 kV and a X-ray tube current of 400 µA. Raw data contain 3-dimensional voxel matrix with a resolution of 51.833 µm per voxel with 16-bit values.

In order to extract the surface area from the raw data, the voxel values need to be classified as solid or non-solid. A common approach is to calculate a threshold by analysing the frequency distribution of the values and using the ISO50 method as a global threshold for surface determination [63,68,69]. Applying this method to the 3-dimensional domain and extracting the surface area yields the entire surface area including the faces inside the hollow struts resulting from the manufacturing process described in 2.1, which will be referred to hereafter as cavities. The inner surface is not considered to participate in solid–fluid interaction with regards to radiative and convective heat transfer. In the present work the specific surface area S_v is defined as the ratio between the external surface and the bulk volume $S_V = A_{out} \cdot V_{bulk}^{-1}$. The application of a global criterion that distinguishes between the inner and outer surface is not possible due to the microscopic holes that connect the outer void to the inner and consequently the cavities to the outer surface.

Therefore, the data were analysed in two-dimensional slides, allowing first the application of adaptive local thresholding as proposed in [70] for boundary determination, and second the classification of

enclosed connected areas into cavities and pores. The thickness of the slide corresponds to the voxel resolution of $res = 51.8$ µm. The calculations were performed using Matlab 2018b [71]. First, the data were read in as two-dimensional arrays in the y–x plane, converted to an 8-bit scale, as visualised in Fig. 6 (a). In the next step, the solid–fluid interface was extracted by calculating the local mean intensity in the neighbourhood of each pixel according to [72], visualised in Fig. 5. If the considered pixel is $p_{min} = 20\,\%$ less than the Gaussian-weighted mean of the surrounding pixels in the area of $n_{pi} = 97$, corresponding to appx. 5 mm, it is assigned to the solid. To eliminate noise effects at the boundaries, all connected areas with size below $n_{min} = 10$ pixels are assigned to noise and deleted. This procedure was repeated in the y- and x-direction and then combined into a matrix, keeping all pixels assigned to solid, as shown in Fig. 6 (b). Inverting the matrix to the fluid assigned to 1, as shown in Fig. 6 (c), allows the connected pixels to be evaluated in terms of their equivalent diameter and circularity and the assignment to pores or cavity. The total porosity including cavities can be calculated by summing all pixels assigned to 1 (as p_{fluid}) and dividing by the total length n_k with $k = x, y, z$, according to Eq. (1).

$$\bar{\Psi}_{CT} = \frac{\sum_{x_{min}}^{x_{max}} \sum_{y_{min}}^{y_{max}} \sum_{z_{min}}^{z_{max}} p_{fluid}}{n_y \cdot n_z \cdot n_x}, \tag{1}$$

In order to extract the outer surface, the interconnected areas with circular shape and equivalent diameter below $d_{eq,min}$ are first assigned to cavities. The threshold $d_{eq,min}$ was set to $d_{eq,min} = 1.29$ mm for KC structures and $d_{eq,min} = 1.55$ mm for the others to match the structural properties of window size and pore size of the structures. Connected areas with an equivalent diameter greater than $d_{eq,max} = 5.18$ mm have been assigned to pores in all cases. Areas with values between $d_{eq,min}$ and $d_{eq,max}$ are further analysed for their eccentricity e and perimeter U. In particular, for the Voronoi and KC structures, the cavities have a more elongated shape compared to the pores, as visualised in Fig. 5. For this reason a filter is applied that removes all connected regions with an eccentricity greater than $e_{max} = 0.95$. For the KC and HK structures, the inner pores can be shaped as a circular ring with an equivalent diameter between $d_{eq,min}$ and $d_{eq,max}$ and a low eccentricity, so they are not affected by the filters applied before. In order to eliminate these shapes without eliminating the areas associated with the pores, the quotient of the perimeter U and the equivalent diameter d_{eq} was calculated, as shown in Fig. 5. For circularly filled areas, this quotient equals π. Therefore, areas with a quotient greater than $\pi \cdot F_{circ}$ with $F_{circ} = 1.3$ were assigned to cavities. All pixels identified as cavities were converted to solid phase. This procedure was repeated in z- and y-direction to avoid cavities that were not detected due to interconnection with pores. The result of this procedure is a matrix as shown in Fig. 6 (d).

An edge detection based on the Roberts algorithm [73] has been chosen for the surface area calculation, providing valuable boundary detection that minimises the thickness of the boundary to one pixel. This algorithm can be applied in all directions $k = x, y$ or z resulting in three different matrices $M_{edge,k}$ with edges assigned to $p_{edge} = 1$. The results obtained for detecting edges in z direction are shown in Fig. 6 (e). The mean specific surface area $\bar{S}_{V,k}$ of the whole structure was determined by summing p_{edge} in all $M_{edge,k}$ divided by the extent of the matrix in number of pixels n_x, n_y, n_z and the resolution res, as

$$\bar{S}_{V,k} = \frac{\sum_{x,y,z=0}^{x,y,z=max} p_{edge,k}}{n_x \cdot n_y \cdot n_z \cdot res}. \tag{2}$$

The mean specific surface area $\bar{S}_{V_{CT}}$ of the samples was calculated from the average of $\bar{S}_{V,x}$, $\bar{S}_{V,y}$ and $\bar{S}_{V,z}$, which also allowed the calculation of the uncertainty $\delta\bar{S}_V$. The local specific surface area along the thickness was then calculated by adding up all pixels in the y–z plane in $M_{edge,z}$, where edge detection was applied perpendicular to the x direction. Divided by the extent of the plane in number of pixels n_y, n_z and the resolution res of the scan, the local specific surface $S_V(x)$ was calculated as shown in Eq. (3).

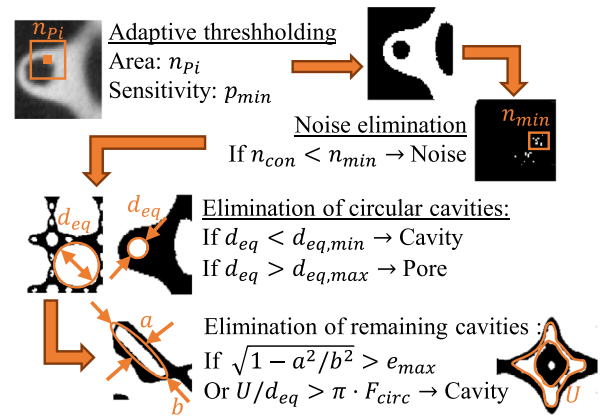

Fig. 5. Schematic explanation of the adaptive thresholding procedure with p_{min}, n_{pi}, noise elimination marking n_{min} and explanation of the subsequent cavity detection procedure with equivalent diameter d_{eq}, eccentricity e and perimeter U of connected areas.

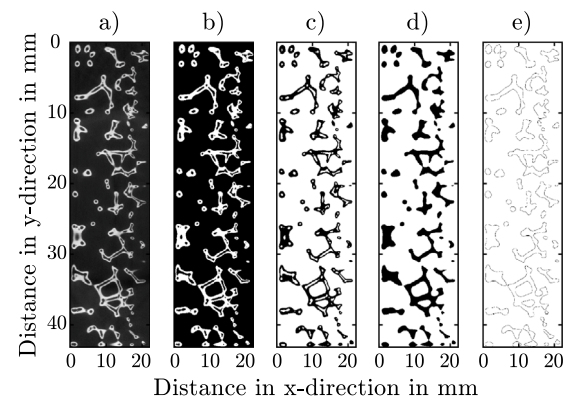

Fig. 6. Illustrations of the progressive procedure of data analyzation for VwG at $z \approx 47$ mm: (a) raw data, (b) binarized with adaptive threshold, (c) after noise filtering and conversion, (d) after elimination of cavities (e) visualisation of edges.

$$S_V(x) = \frac{\sum_{y_{min}}^{y_{max}} \sum_{z_{min}}^{z_{max}} p_{edge}}{n_y \cdot n_z \cdot res}. \tag{3}$$

2.3.2. Specific surface determination of 3D-models

As described in 2.1, the structures studied in the present work are based on a 3D model that was designed prior to the construction of the polymer template. The local and mean specific surface area of the 3D model were examined to validate the data obtained from the CT scan and as a manufacturing quality control. Models are available for the Voronoi structures, the Kelvin cell structures and the Hendecahedron structure. Only a partial extract of stacked unit cells is available for KC, opt. KC and HK. The external dimensions are 20 mm x 12.9 mm x 20 mm for KC and 22.2 mm x 15.2 mm x 22.2 mm for opt. KC, which represents six stacks of three unit cells each. The HK model extends over 26.4 mm x 31.4 mm x 21.2 mm. For the Voronoi, a representative volume of 30 mm x 30 mm x 20 mm was chosen, as shown in Fig. 3. In order to determine the local and mean specific surface area, the models were analysed using the ParaView tool library [74] implemented in a Python script. The models were provided by EngiCer SA. The mean specific surface $\bar{S}_{V_{model}}$ was calculated by summing the area of all triangles and dividing by the total volume. To calculate the local specific surface $S_{V_{model}}(x)$ the model was sectioned along a plane perpendicular to the x-direction, incrementing in $\delta x \approx res$ from x_{min} to x_{max}. The local

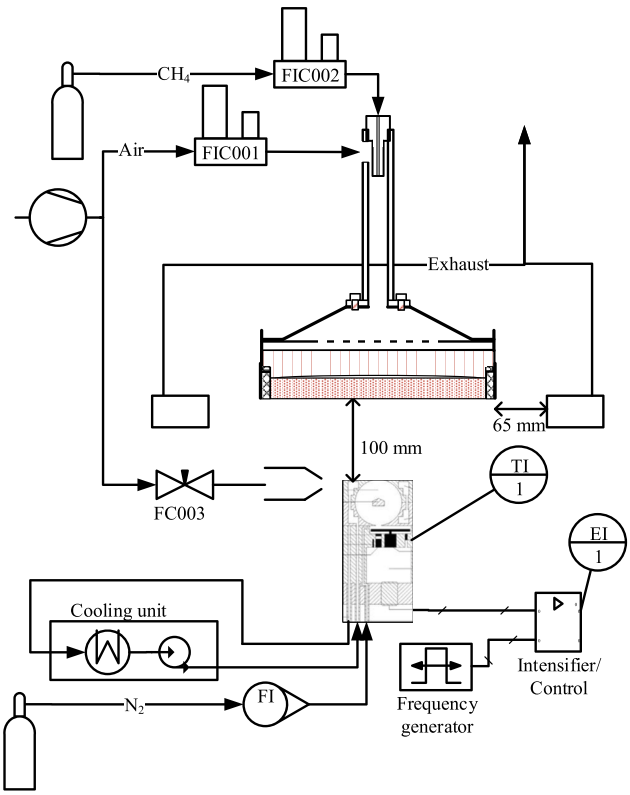

Fig. 7. Schematic overview of the test rig with porous burner, radiometer, exhaust extraction and peripheral measurement equipment and actors.

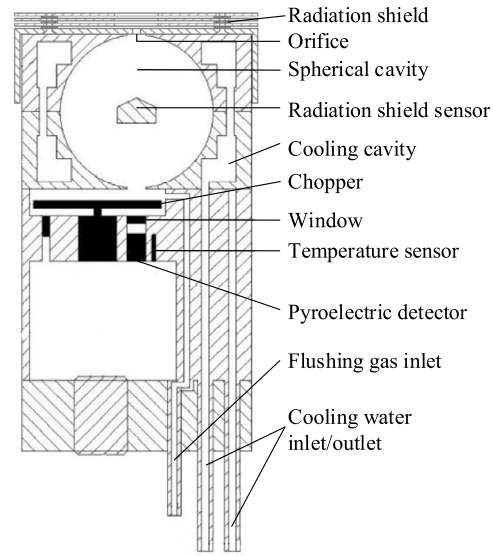

Fig. 8. Schematic overview of radiometer assembly adapted from [75].

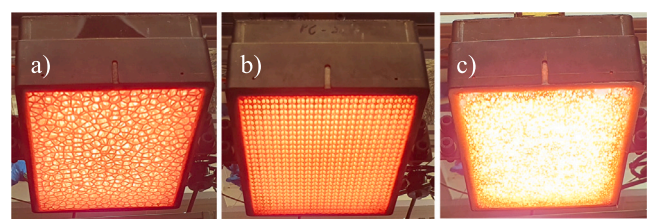

Fig. 9. Photograph of burner in operation at 1000 kW m^{-2} with porous inlays in (a) Voro (b) TK and (c) RF20 geometry.

specific surface area was calculated in a loop by extracting the area of all triangular surfaces up to the plane, subtracting the area determined in the previous loop and dividing by the volume of the section, which corresponds to the total area in the y-z-direction multiplied by δx. The procedure was validated by comparing the average of the local specific surface area values $S_{V_{model}}(x)$ with the specific surface area of the entire model $\bar{S}_{V_{model}}$, showing complete agreement.

2.4. Experimental methods

The radiant power of the burner has been measured on a designated test rig using a radiometer for the measurement of the irradiance at discrete positions on a measurement plane parallel to the burner surface as suggested in standard DIN-EN 419 [75]. Mital et al. [41] have also shown that measuring radiation intensity at multiple points is the most accurate and repeatable method to measure the irradiance of RPB's.

2.4.1. Test rig

As shown in Fig. 7, the burner described in 2.1 is mounted radiating towards the ground (see Fig. 9). The air fed to the burner is supplied by a Kaeser CSD 122 T SFC compressor, dried to a dew point of 278 K and then metered and controlled using a FIC001 mass flow controller (Bronkhorst High-Tech B.V.). Methane with a purity of ≥99.5 mol% is used as fuel, supplied from a pressurised gas cylinder and metered and controlled with a mass flow controller FIC002 (Bronkhorst High-Tech B.V.). In order to avoid shadowing, the flue gas is exhausted on two sides below the burner at a distance of 65 mm.

Irradiance is measured with a radiometer as shown in Fig. 8 mounted on a two-dimensional traverse system and designed in accordance with [75].

Radiation enters through an aperture of 2 mm diameter and is reflected in a gold-plated spherical cavity before being measured by a pyroelectric detector LIE-312-70 (InfraTec GmbH). The detector has a silica window. A frequency controlled chopper is implemented to periodically shade the detector at a frequency of 70 Hz. The temperature change between a reference temperature and the one produced by the radiation are measured. The reference temperature is measured by a PT100 sensor at the detector. The cavity and housing are cooled with cooling water supplied by an ECO 415 thermostat (Lauda GmbH) to provide a reference temperature of 293 K. In addition, the sphere is purged with 25 l/h (FC003) nitrogen to enforce repeatable conditions. The detector signal is amplified to a range of 0 V to 10 V with a sensitivity of 3 mV and a damping of 1000 ms (EI-1). It is transmitted to the data acquisition system together with the temperature (TI-1). Convective cooling of the upper part with pressurised air and a three-layer radiation shield are used to prevent rapid heating of the instrument. The radiometer was calibrated in a spherical blackbody cavity with an inner diameter of 300 mm and an orifice of 70 mm diameter. The detector signal was recorded in four repeated measurements at four sphere temperatures of T_{sphere} = 673 K to 1273 K, corresponding to radiation intensities calculated with $\dot{E} = \sigma \cdot T^4_{sphere}$ of about 10 kW m^{-2} to 150 kW m^{-2}. A calibration line following $\dot{E} = a \cdot U + b$ was fitted to the data and used to convert the signal measured in voltage U to irradiance $\dot{E}$.

2.4.2. Procedure

The irradiance is measured at several discrete points in a plane 540 mm by 490 mm parallel to the burner surface at 100 mm intervals to calculate the total radiant flux by integrating an approximation function fitted to this distribution. Explanation of the theoretical background of this procedure is elucidated in Section 3. The measurement grid size is sufficient to capture the radiant flux of the burner, as the signal value at the edges is < 5 % of the maximum value for each thermal power and structure investigated.

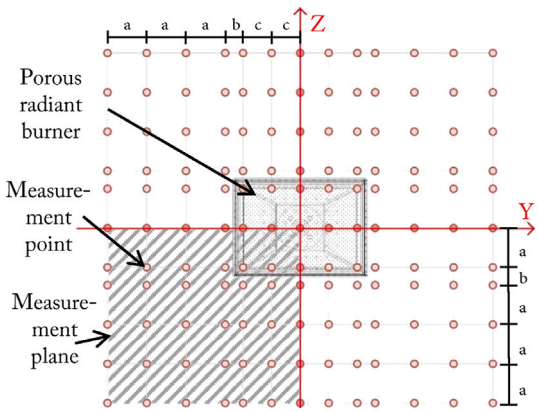

Fig. 10. Sketch of the applied measurement grid with the porous radiant burner shown scaled together with measurement points marked in dots and the measurement plane shaded.

The distances shown in Fig. 10 refer to $a = 55$ mm, $b = 25$ mm and $c = 40$ mm. Symmetry was demonstrated by determining the irradiance at all points along the y and z axes for each structure and specific power. To calculate the radiated power, irradiance values are taken at all the measurement points marked in the shaded area in Fig. 10. Stationary conditions are defined by the radiometer reference temperature limited by 292.5 K to 293.5 K and the signal limited by a slope below 0.05 V s^{-1}. The value is recorded over 15 s and subsequently averaged.

The burner is operated at a specific thermal power between $P_A = 600\,\mathrm{kW\,m^{-2}}$ to $1000\,\mathrm{kW\,m^{-2}}$ and a constant equivalence ratio of $\phi = 0.7$. This is the limiting condition for stable long term operation of radiant burners with porous SiSiC inlays ensuring that the solid temperature within the structure remains below the material limit, whilst being as high as possible to maximise irradiation.

As described in Section 3, the distribution of irradiance in the measurement plane can be described by a cumulative density function. Applying the function in two dimensions and allowing for the adaptation of the mean and variance to the measurement data by an algorithm, Eq. (8) changes to

$$F(z,y) = \frac{1}{4}\cdot B\cdot\left[1+erf\left(\frac{z-C}{D\sqrt{2}}\right)\right]\left[1+erf\left(\frac{y-E}{G\sqrt{2}}\right)\right]. \tag{4}$$

The parameters C, D, E, G are fitted using a Levenberg–Marquardt algorithm to minimise $\sum|F(y,z)-\dot{E}_i|^2$, where $\dot{E}_i$ represents the measured data. The coefficient B is set to the maximum measured value for all investigated structures and thermal power. The radiated power $\dot{Q}_{rad}$ is obtained by numerical integration of $F(z,y)$ over z and y and multiplication by four. This takes into consideration the evaluation of only a quarter of the measured area.

As suggested in [75] and carried out in [41] the radiated power can be calculated by multiplying the irradiance by corresponding discrete subareas splitting the measurement plane into tiles. This procedure does not follow the physically justified distribution of radiation and is therefore less accurate than the approximation to the function in Eq. (4).

Deviation due to the data fitting can be expressed via the square of the multiple correlation coefficient as shown in Eq. (5).

$$R^2 = 1-\sum_{i=0}^{n} w_i(\hat{y}_i-\bar{y}_i)^2\cdot\left(\sum_{i=0}^{n} w_i(y_i-\bar{y})^2\right)^{-1} \tag{5}$$

3. Theory

Irradiance of a planar surface increment is defined as the flux of energy per unit solid angle and per unit area normal to the rays. The total energy E, emitted from a surface area dA into all directions is defined as an integral of radiant flux $I(r,\Omega)$, over the solid angle Ω and the projected area A_P as

$$E(r) = \int_{A_p}\int_{\Omega} I(r,\Omega)dA_p d\Omega. \tag{6}$$

The infinitesimal solid angle is denoted as $d\Omega = \sin(\theta)d\theta d\psi$ where θ and ψ represent the angles to the normal in both directions. Integrating this expression over these two angles leads to a function of the projected area and the distance $d\Omega = dA_p\cdot s^{-2}$ [76]. By expressing the projected area with $dA_p = dA\cdot\cos(\theta)$, the total energy leaving an infinitesimal surface i for a finite j is defined as follows.

$$E(r_i\to j) = I(r_i)\cdot\frac{\cos(\theta_i)\cdot\cos(\theta_j)}{s^2}dA_i dA_j \tag{7}$$

Simplifying the problem by assuming two parallel facing infinite surfaces, the angles to the normal are equal $\theta_j = \theta_i = \theta$ and thus the energy transported is proportional to $\cos(\theta)^2\cdot s^{-2}$. The distribution of a cosine function is comparable with the normal probability density function [77]. In a study by Warsza et al. [78], it was found that a distribution based on $\cos(x)^2$ deviates to the normal distribution by $\pm 2\,\%$ over the range of a full period. As a good approximation, the normal distribution can therefore be used to describe the radiation from an infinite area to a infinite area in parallel. To express the distribution from an finite surface to a infinite area the standard normal cumulative distribution function in Eq. (8) has to be used. Whereas μ corresponds to the mean and σ^2 to the variance of the distribution.

$$F(x) = \frac{1}{2}\left(1+erf\left(\frac{x-\mu}{\sigma\sqrt{2}}\right)\right) \tag{8}$$

Assuming two parallel plates with area A and average emissivity ε the radiant flux $\dot{Q}_{rad}$ in Eq. (9) can be derived from Eq. (6).

$$\dot{Q}_{rad} = \sigma\cdot\varepsilon\cdot A\left(T_{surf}^4 - T_\infty^4\right) \tag{9}$$

The surface temperature of the plate is represented by T_{surf}, whilst T_∞ refers to the surrounding temperature [79].

The amount of chemically bound energy in the fuel emitted via thermal radiation is quantified in terms of the radiation efficiency. Radiation efficiency, as defined in the Eq. (10), refers to the radiated power relative to the thermal power, expressed as a function of fuel mass flow $\dot{m}_{Fuel}$ and net calorific value H_u.

$$\eta_{rad} = \frac{\dot{Q}_{rad}}{\dot{m}_{Fuel}\cdot H_u}\cdot 100\% \tag{10}$$

In order to facilitate a comparison of radiant burners with varying radiation surface areas, the thermal power is expressed as specific power by dividing by the planar surface area $P_A = \dot{m}_{Fuel}\cdot H_u\cdot A^{-1}$.

In the present work, the operating principle of the burner is unidirectional, with the latent heat of the flue gas and the radiation leaving the system in parallel. Due to the convective heat transfer between solid and fluid the flue gas temperature cannot fall below the solid surface exiting the structure. As a result, the limiting condition is represented by the equilibrium between the exhaust gas temperature and solid surface temperature. The thermodynamics of the entire system are considered and an enthalpy balance, presented in Eq. (11), is maintained at the system boundaries.

$$\begin{aligned}\dot{m}_{Fuel}\cdot H_u^0 + \dot{m}_{tot}\cdot\int c_u(T)\cdot\left(T_{in}-T_{ref}\right) = \\ \dot{Q}_{rad} + \dot{m}_{tot}\cdot\int c_c(T)\cdot\left(T_{gas}-T_{ref}\right).\end{aligned} \tag{11}$$

T_{gas} refers to the temperature of the exhaust gas, T_{ref} to the reference temperature of 273.15 K and T_{in} is the temperature of the unburned mixture. The specific heat capacity is calculated for the corresponding temperature and composition of the unburned $c_u(T)$ and burned $c_c(T)$ gas. An air composition of 79 % N_2 and 21 % O_2 as well as pure CH_4 as fuel were assumed. The burner design and stabilisation method is characterised by intensive radiation output and low pollutant, as

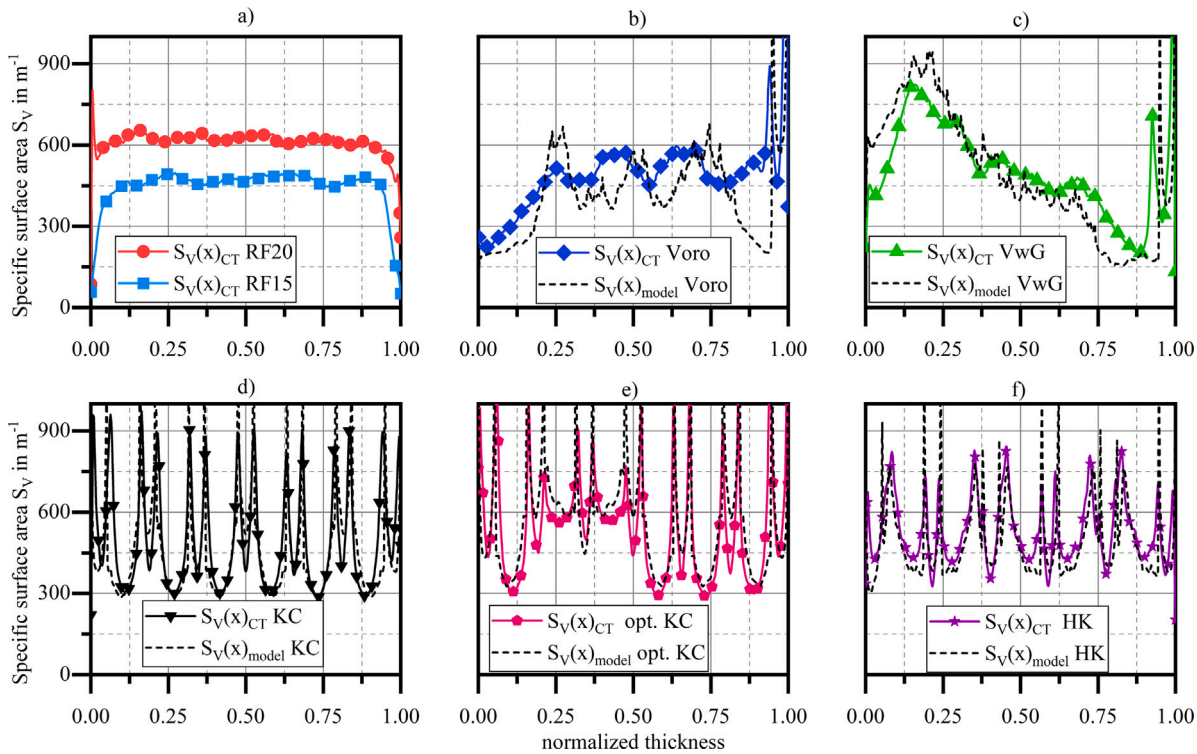

Fig. 11. Local specific surface area $S_V(x)$ over burner thickness in x-direction normalised (nt) for (a) RF15 and RF20, (b) Voro, (c) VwG, (d) KC, (e) opt. KC, and (f) HK. (For interpretation of the references to colour in this figure legend, the reader is referred to the web version of this article.)

demonstrated in previous experiments [48]. This suggests that combustion efficiency is high and therefore it is justified to assume complete conversion to CO_2 and H_2O. Coefficients for the calculation of $c_u(T)$ and $c_c(T)$ were taken from [80]. In consideration of the design of the burner utilised in this study, the transfer of heat from the gas phase to the solid phase proceeds in a parallel direction relative to the radiation emitted into the surrounding environment. It follows that the maximum temperature at the outlet of the emitter is constrained by the temperature of the gas, which allows for the setting of a limiting solid temperature of $T_{solid} = T_{gas} = T_{equ}$. For a fuel with a given composition, a radiator with a constant surface emissivity and a flat surface Eq. (11) has a specific value for T_{equ}. The solution can be determined graphically or using a root-determination method.

Table 1
Mean specific surface values determined from the CT-scan and 3D-model, Thickness of structure Δx resulting from the CT-scans and physically measured (Real), Porosity determined from CT-scans via equ. (1).

	CT-Scans			3D-Model		Real
	Δx [mm]	$\bar{S}_{V_{CT}}$ [m^{-1}]	Ψ_{CT} [%]	Δx [mm]	$\bar{S}_{V_{model}}$ [m^{-1}]	Δx [mm]
RF20	19.54	622.7	83.8	–	–	19.69
RF15	15.86	444.8	84.3	–	–	15.43
Voro	20.83	504.4	83.5	21.1	425.1	20.86
VwG	20.85	514.1	82.6	21.1	498.6	21.02
KC	21.20	508.3	83.5	22.2	477.7	21.05
opt.KC	21.09	555.9	81.0	20.0	587.3	21.12
HK	20.89	501.5	82.2	21.2	499.5	20.84

4. Results and discussion

The specific surface area of structures is identified as a key factor influencing radiation output. This is determined through the analysis of samples and 3D models, with the results presented in the following section. In Section 4.2, the results of the radiation efficiency measurement and the uncertainties are discussed, compared to the references in literature and theory. The final Section 4.3 concludes this chapter by the relation between the mean specific surface value and radiation efficiency.

4.1. Specific surface area

Mean values for specific surface areas obtained from the CT scan $\bar{S}_{V_{CT}}$ and calculated from the 3D model $\bar{S}_{V_{model}}$ are presented in Table 1 for all structures examined.

The values obtained from the CT-scan range from 445 m^{-1} to 623 m^{-1}, while the foam structures encompass this range. The $S_{V_{CT}}$ value agrees well with structures of Al_2O_3 having 10 PPI and $\Psi = 85\%$, as analysed by Garrido et al. [81], with a value of 629.3 m^{-1}. Voronoi structures, HK and KC values are displayed within around 500 m^{-1}. Compared to this, the opt. KC exhibits higher values but do not reach those of the RF20. Besides the foam structures, the values are compared with the specific surface values obtained from the 3D models. For validation the specific surface area of KC can be compared to the values obtained from Wieland et al. [46] with $S_V = 471$ m^{-1}, which is in good agreement with $S_{V_{model}}(KC)$.

Besides calculating the mean specific surface area of the entire structure $\bar{S}_V$, the local specific surface area over the thickness of the burner in the x-direction $S_V(x)$ was calculated to further evaluate the differences between the porous structures. Values for the local and mean specific surface area, calculated from the scans as explained in Section 2.3.1, have been compared with the local and mean specific surface from the model evaluated for HK, KC and Voronoi structures, as detailed in Section 2.3.2. The results are presented in Fig. 11 (b) to (f), plotted against the normalised thickness $x \cdot (x_{max} - x_{min})^{-1}$ (nt) in order to facilitate comparison between the results of the 3D model and CT scans with differing structure thickness. The foam structures' specific surface distribution, as shown in Fig. 11(a), is characterised by a uniform distribution along the thickness. Table 1 has already demonstrated that RF15 has lower values than RF20. In the flow

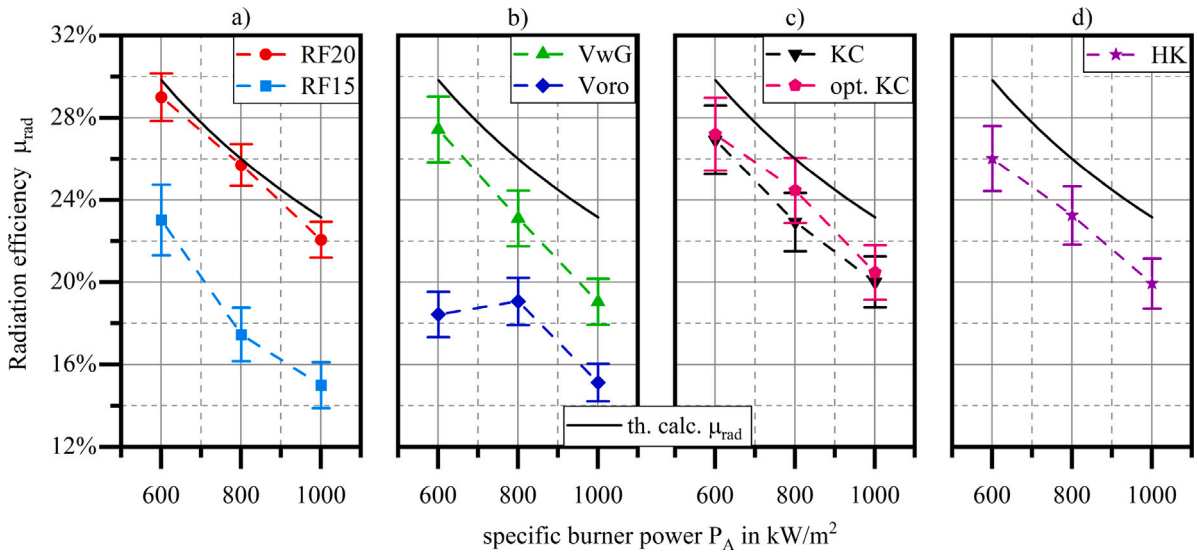

Fig. 12. Radiation efficiency measured for the investigated (a) foam, (b) Voronois, (c) kelvin cell and (d) hendecahedron structures as a function of the specific burner power compared to the theoretical calculated limiting radiation efficiency (th.calc. η_{rad}) for $\varepsilon = 1.0$ and $\phi = 0.714$ as solid line.

direction a continuous increase and decrease in $S_V(x)$ are observed for Voro and VwG respectively. Both structures exhibit an increase in $S_V(x)$ until reaching a normalised thickness of 0.25 for Voro or 0.125 for VwG, corresponding to the design with unconnected struts at x_{min} in the z–y-plane, as illustrated in Fig. 3. The subsequent even progression shows a decrease in $S_V(x)$ from $800\,\mathrm{m}^{-1}$ to $200\,\mathrm{m}^{-1}$ between 0.125 and 0.85 for the VwG. For Voro the value levels between $470\,\mathrm{m}^{-1}$ to $560\,\mathrm{m}^{-1}$ up to 0.85 normalised thickness. The trend for VwG aligns with the predicted gradient in pore density. Peak values exceeding $900\,\mathrm{m}^{-1}$ reaching the highest thickness occur due to connected struts in the z–y plane at x_{max} (nt = 1).

Periodic fluctuations in $S_V(x)$ are observed, ranging from $300\,\mathrm{m}^{-1}$ to $1000\,\mathrm{m}^{-1}$ for KC and from $300\,\mathrm{m}^{-1}$ to $800\,\mathrm{m}^{-1}$ for HK. The double local maxima in the KC distribution correspond to the periodic distribution of the small rectangular strut network, which is situated every 3.3 mm (0.15 nt) parallel or perpendicular to the y–z-plane. These periodic fluctuations lead to a decrease in $S_V(x)$ to $450\,\mathrm{m}^{-1}$ due to a decreased perimeter of the inner window size with increasing nt. The occurrence of local minima between the double peaks is attributed to the presence of open large windows. The elimination of these drops between 0.1 nt to 0.5 nt demonstrates the optimisation of the KC to opt. KC. This effect is reflected in the mean values as a 10 % increase in $\bar{S}_{V_{CT}}$.

Two local maxima in the progress of $S_V(x)$ in HK occur at 0.375 and 0.75. They represent a significant number of struts without a joint, corresponding to a high value of $800\,\mathrm{m}^{-1}$. The value drops to $350\,\mathrm{m}^{-1}$ due to a rectangular shaped strut lattice parallel to the z–y plane as in KC structures. Two maxima distributed every 7.8 millimetres (0.4 nt) starting at 0.2 nt correspond to struts perpendicular to the z–y plane with a low local specific surface area of $320\,\mathrm{m}^{-1}$.

The specific surface area extraction procedure was evaluated in terms of the associated uncertainties, which were addressed through the implementation of a simplified geometry and a comparison with the results of physical measurements and the evaluation of the 3D models. The validity of the threshold procedure was verified by comparing the thickness of the real structure with the thickness calculated by $\Delta x = (p_{edge,max}(x) - p_{edge,min}(x)) \cdot res$, as shown in the Table 1. Deviations were found to be within the acceptable range of physical measurement uncertainty. In order to assess the uncertainties arising from the removal of internal porosity using the method described in 2.3.1, the results of the fabricated structures are compared to the 3D models. The uncertainty of the edge detection method was assessed by its application to a volumetric body with an analytical solution for the surface area. A sphere with a diameter equivalent to the structure thickness was modelled and transferred to a three-dimensional matrix of pixels with a resolution corresponding to the CT scans. One slice with a thickness of *res* and varying in position over the diameter was analysed. The calculated surface area for this slice deviates between −2.75 % to 2.56 % from the analytical solution of the perimeter. Calculating the surface area of the entire sphere by adding up all edge pixels results in a deviation from the analytical solution of 0.028 %. The mean specific surface value's uncertainty was obtained by calculating the sample standard deviation of the directional average of $\bar{S}_{V_{CT}}$ in all directions k. The result is presented in Table 2. Highest deviations could be found for the foam structures, moderate for Voronoi and HK and the lowest for the KC structures.

Table 2
Relative sample standard deviation of calculated mean specific surface area $\bar{S}_{V_{CT}}$ for the structures examined.

Structure	RF20	RF15	Voro	VwG
$\sigma_{\bar{S}_V}$	±6.6 %	±7.11 %	±3.36 %	±3.15 %
Structure	KC	opt. KC	HK	
$\sigma_{\bar{S}_V}$	±2.7 %	±2.35 %	±3.43 %	

4.1.1. Comparison of 3D-model and CT-scan

The results are compared with the 3D models of the Voronoi, KC and HK structures to validate the specific surface area extraction procedure from CT data and to assess whether the template properties are as desired based on predicted manufacturing behaviour. The results of the mean values are presented in the Table 1 and the results of $S_V(x)$ are shown in Fig. 11(b) to (f). Considering the mean values of HK, the average surface areas $\bar{S}_{V_{model}}$ and $\bar{S}_{V_{CT}}$ are in very good agreement. Upon investigating the progress, the peaks attributed to struts that are perpendicular to the z–y plane are more distinct for the 3D-model, whereas the local minima attributed to the rectangular shaped geometries are more pronounced in the CT-scan due to closed windows resulting from the manufacturing process. The same phenomena can be observed for KC structures with local minima periodically distributed every 3.4 mm (corresponding to 0.16 normalised distance), which are more pronounced for the scans compared to the model, as seen in Fig. 11 (d). Differences in the distribution of KC at low and high normalised thicknesses between the model and the scans arise from variations in thickness and normalisation. Overall, a higher $\bar{S}_{V_{CT}}$ for

KC in comparison to $\bar{S}_{V_{model}}$ is observed. This is attributed to increased strut thickness and is evidenced by wider peaks in $S_V(x)$.

The opt. KC structure exhibits more pronounced local maxima in $S_V(x)_{model}$ compared to the scan up to $1600\,\mathrm{m}^{-1}$. These are not observed in $S_V(x)_{CT}$ since the curve progression is the result of an averaging over a large cross-sectional area, which is not strictly parallel to the z–y-plane. Lower $S_V(x)_{CT}$ than $S_V(x)_{model}$ indicate a smaller strut diameter of the manufactured structure as intended. Furthermore, the manufacturing process fails to reproduce the sharp edges between the closed windows and the struts (refer to Fig. 2 b)), resulting in a smoothed distribution and lower average values by 5.3%.

Regarding the Voronoi structures, the slight discrepancy between $\bar{S}_{V_{CT}}$ and $\bar{S}_{V_{model}}$ for VwG compared to Voro is a result of compensating negative and positive differences, which are shown in Fig. 11 (c). Voro, on the other hand, shows a decrease to $200\,\mathrm{m}^{-1}$ at a thickness of 0.9 in $S_V(x)_{model}$. This decrease is not as pronounced in $S_V(x)_{CT}$ due to the larger section analysed in the CT scan, as explained in Section 2.3.2. This discrepancy leads to a remarkable decrease of 10% for $\bar{S}_{V_{model}}$ in comparison to $\bar{S}_{V_{CT}}$. The peaks observed in $S_V(x)_{CT}$ at x_{max} correlated with $S_V(x)_{model}$ which validates the presence of high $S_V(x)$ at x_{max} caused by struts parallel to the z–y plane. Summarised, a good agreement was observed between the local and mean specific surface area of the manufactured structures and the corresponding 3D models. This emphasises the predictability of geometric properties and the reproducibility of structures produced by hybrid additive manufacturing.

4.2. Radiation efficiency

The radiated power of all structures was measured on a dedicated test rig in accordance with the procedure described in Section 2.4. Additionally a limiting theoretical radiation efficiency for a radiating planar surface with a temperature of $T_{surf} = T_{equ}$, a constant emissivity of $\varepsilon = 1.0$ and area A as given in Section 2.1 was derived from equ. (9) and (10) for varying specific power P_A. The equilibrium limiting surface temperature T_{equ} can be determined from (11) for $T_{in} = 293\,\mathrm{K}$ by means of Newton's method. The limiting efficiency is plotted against the specific burner power P_A together with the measured radiation efficiency η_{rad} of the investigated structures in Fig. 12. Results show values ranging from 18.4 % to 29 % for the lowest specific power of $600\,\mathrm{kW\,m^{-2}}$, to 15 % to 22 % for the highest specific power of $1000\,\mathrm{kW\,m^{-2}}$. For all structures, despite Voro, the radiation efficiencies decrease almost linearly with increasing P_A. The highest values were observed for RF20, approaching the limit $\eta_{rad,equ}$. For $600\,\mathrm{kW\,m^{-2}}$ the lowest value was measured with Voro and for the remaining P_A with RF15.

For the lowest P_A KC, VwG and opt. KC display comparable values within the range of 26.9 % to 27.1 %. However, for HK, η_{rad} is approximately 1 % lower, while RF15 yields a η_{rad} of 23 %. Conversely, for $800\,\mathrm{kW\,m^{-2}}$, HK, VwG and KC exhibit similar values in the range of 22.9 % to 23.4 %, whereas opt. KC is 1 % higher. RF15, on the other hand, drops 1.5 % below Voro with $\eta_{rad} = 19\,\%$. For the highest power of $1000\,\mathrm{kW\,m^{-2}}$, the values for HK, VwG, KC, and opt. KC are almost similar, ranging from 19 % to 20.5 % with overlapping uncertainties. Voro and RF15 have almost identical values of around 15 %, with a difference of only 0.1 %. The radiation efficiency of the foam structures exhibited the highest and lowest mean specific surface area values at comparable specifications from the manufacturer. This indicates a broad spectrum of qualitative variations in the geometrical properties of the manufactured product, which in consequence yield a correspondingly broad range of efficiency values. The reduction in radiation efficiency with rising specific power can be elucidated by the calculated theoretical radiation efficiency shown in Fig. 12. Additionally this finding has been confirmed and reinforced in [23,44]. The data indicates that the irradiance increases with higher thermal power, although not in the same proportion. Stelzner et al. [38] have identified that the distance between the flame trap and the flame front increases with increasing power. In addition to an increase in flow velocity and thus intensified heat transfer, this lift-off also leads to a shortening of the distance in which heat is transferred from the gas phase to the solid phase. This results in a reduction of the zone with the highest solid temperature. Wieland et al. [46] conducted numerical analyses of identical burner assemblies, enabling in-depth examination of the complex interaction between heat transfer within the structure and irradiation to the ambient. The results demonstrated a reduction in radiation efficiency with increasing thermal power, as well as a shift of the flame front and the maximum solid temperature towards the burner outlet. Furthermore, the convective heat transfer scales linearly with the surface area. This is analysed in the present study on the basis of the local and mean specific surface area. As illustrated in Fig. 11, Voro is deficient in available surface area near the flame trap. At low thermal power and high gas temperature, the heat transfer from the gas phase to the solid is expected to be enhanced near the flame trap, where Voro has a smaller surface area.

The results presented are also comparable with experimental studies in the literature. Unfortunately, the operating conditions and material properties of the burner used in this study do not match the radiant power measurements obtained using pyrometer technology in the literature. Mital et al. reported a comparable $\eta_{rad} = 27\,\%$ for SiC-coated cordierite with an almost similar power of $630\,\mathrm{kW\,m^{-2}}$ and a higher equivalence ratio of $\phi = 0.9$. In contrast, in Maznoy's study, metallic Ni–Al structures had a radiation efficiency of 29 % for a power of $297\,\mathrm{kW\,m^{-2}}$. Comparable material and structure to the present study was utilised by Caetano et al. who measured a $\eta_{rad} = 20\%$ and 17.8% at $P_A = 738\,\mathrm{kW\,m^{-2}}$ and $\phi = 0.7$ with a 10PPI and 20PPI SiC foam structure, which is similar to the outcomes obtained with foams in the present research. Radiation efficiencies for a similar setup and material were obtained by measuring surface temperature and were published by Keramiotis et al. [44]. Efficiencies range from 32 % to 25 % at $600\,\mathrm{kW\,m^{-2}}$ to $800\,\mathrm{kW\,m^{-2}}$ and $\phi = 0.833$, which is slightly higher than the values obtained for RF20 due to the higher equivalence ratio. Results obtained from Devi et al. [82], who investigated a SiC random foam, show a radiation efficiency of 19 % at $884\,\mathrm{kW\,m^{-2}}$ for Biogas combustion at $\phi = 0.9$, which is again comparable to the results obtained with the RF15. Numerical investigations by Wieland et al. on KC structures in a two-layer burner setup resulted in radiation efficiencies between 42 % to 37 % for $600\,\mathrm{kW\,m^{-2}}$ to $800\,\mathrm{kW\,m^{-2}}$ at an equivalence ratio of $\phi = 0.91$. Noticing the discrepancy in the equivalence ratio, which leads to an absolute difference of 10% according to [44], the absolute difference in radiation efficiency results in 3 % to 4 %. Accounting for the absence of transversal heat losses in the numerical calculation, the results presented by Wieland et al. are in good agreement with the measured values for the KC structure.

Measurement of a quarter of the area, errors in repeatability and data processing represent the major sources of uncertainty for the radiated power measurements in this study. To evaluate uncertainty due to repeatability, major axis readings were taken at P_A of $800\,\mathrm{kW\,m^{-2}}$ prior to each measurement. Relative uncertainties in intensity decrease at high radiation intensities. Applying the mean uncertainty across all intensities leads to larger or similar quantities of uncertainty for radiated power in comparison to applying uncertainties as a function of the intensity for each discrete measurement point. The uncertainty arising from assuming symmetry was evaluated for a single structure by measuring the radiation intensity at all points shown in Fig. 10. The radiated power resulting from post-processing the readings in all four quadrants of the grid separately was compared. The resulting relative deviation is $\sigma_{rel} = \pm 3\,\%$. Without differentiating between deviations resulting from repeatability, this uncertainty will henceforth be included within the deviation determined from repeatability. The relative uncertainties for all investigated structures are presented in Table 3. These uncertainties correspond to the repeatability applicable to the total power determined. Comparable values for uncertainty were determined by Mital et al. with ±5% [41], Speyer et al. [39] with

Table 3
Relative standard deviation of measured radiated power for the structures examined.

Structure	RF20	RF15	Voro	VwG
σ_{rad}	±3.9 %	±7.4 %	±6.0 %	±5.8 %
Structure	KC	opt. KC	HK	
σ_{rad}	±6.1 %	±6.0 %	±6.5 %	

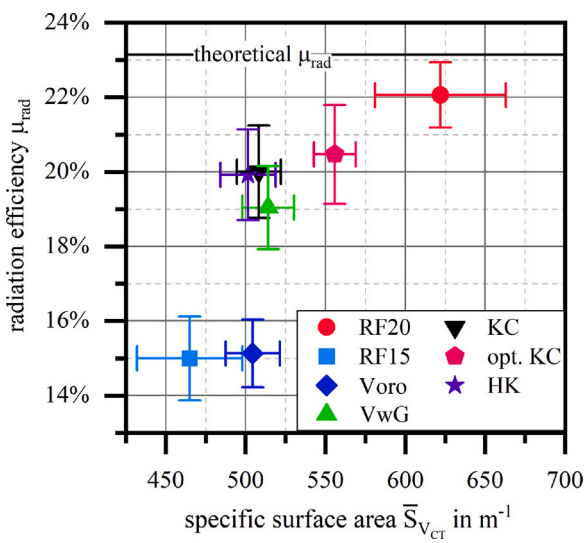

Fig. 13. Measured radiation efficiency for $1000\,\mathrm{kW\,m^{-2}}$ vs. corresponding mean specific surface area from Table 1, structures distinguished by symbols according legend. Theoretically calculated radiation efficiency for $\phi = 0.7$, $P_A = 1000\,\mathrm{kW\,m^{-2}}$ and $\varepsilon = 1.0$ shown as horizontal black line.

±10% in a one point measurement and Caetano et al. [20] of ±1% from fluctuations in the captured signal not taken into account the repeatability. Deviations between the regression and the measured data points were calculated using equ. (5) for each structure and specific burner power. Values from correlation and measured values show strong correspondence above $R^2 = 98\%$.

4.3. Relation between S_V and η_{rad}

The structures studied vary in mean specific surface area and radiation efficiency over a wide range. Fig. 13 demonstrates the relation between η_{rad} and $\bar{S}_{V_{CT}}$, showing the measured η_{rad} for $1000\,\mathrm{kW\,m^{-2}}$, with the structures marked with symbols according to the legend. It can be observed that the radiation efficiency increases with the mean specific surface area of the porous ceramic structure, with the exception of the Voronoi structures. The distribution asymptotically approaches the maximum marked by the theoretical radiative efficiency. The non-linear distribution can be attributed to the complex relationship between flame stabilisation within the structure and the heat transfer between the gas and solid phases studied in detail in [46]. Furthermore, expressing the relationship in terms of the mean available surface area does not adequately account for the inhomogeneous surface distribution along the flow. The wide distribution and non-linearity also highlight the necessity of treating radiant porous burners as volumetric radiant emitters, as demonstrated by numerical investigations in [47]. The foam structures with identical pore density, as given in the data sheet, show the highest increase, with 39.9 % in $\bar{S}_{V_{CT}}$ from RF15 (blue square) to RF20 (red circle). This results in a relative increase of 40.3 % in $\dot{Q}_{rad}$ across all P_A values, which could potentially decrease $\dot{m}_{fuel}$ by 60 % while achieving the same radiated power. The impact of surface distribution on radiative power is demonstrated through the Voronoi structures' comparison. The VwG structure (green triangle) and the Voro structure (blue rhombus) have comparable mean specific surface areas, but differ in the distribution of the local specific surface area along the flow direction, as visualised in 11 (b) and (c). This leads to a 30% increase in η_{rad}. While RF15 exhibits lower average values in $\bar{S}_{V_{CT}}$ than Voro, its homogeneously distributed surface area result in a comparable η_{rad}. This result also suggests that the triangular strut geometry has a beneficial effect on thermal transfer within the porous structure. Concerning the periodically distributed structures KC and opt. KC exhibit a 10% rise in $\bar{S}_{V_{CT}}$, leading to a 3.3% increase in η_{rad} for all examined P_A. It proves that this structures can be optimised regarding radiative output by selectively increasing the local specific surface area.

5. Conclusions

The radiation efficiency of a radiant porous burner following the two-layer design was measured at a constant equivalence ratio of $\phi = 0.71$ and at specific powers of $P_A = 600, 800$ and $1000\,\mathrm{kW\,m^{-2}}$. Seven different geometrical structures produced by the replica method were investigated, including state of the art foam structures as well as regular and random distributed lattice structures. For the characterisation of the structure geometry, a computed tomography scan followed by custom data analysis was used to derive the specific surface area. The main achievements can be summarised as follows:

- A standardised measurement technique has been successfully adapted for high power density porous radiant burners, allowing for the measurement of radiated power for a specific burner power of up to $1000\,\mathrm{kW\,m^{-2}}$ and thus ensuring reproducibility of the results presented.
- The highest mean specific surface area and thus radiation efficiency was observed for the foam structure, which approached the limiting radiation efficiency of 30 % at $P_A = 600\,\mathrm{kW\,m^{-2}}$.
- Structures manufactured by additive hybrid manufacturing with regular strut distribution exhibit lower mean specific surface area and radiation efficiency compared to the 10 PPI foam.
- Additionally a comparison between the local and mean specific surface area of the preliminary design model and the manufactured ceramic structures are in good agreement, indicating a high level of predictability in the hybrid additive manufacturing process and a corresponding level of repeatability in the geometric properties produced.
- The directed increase in local and mean specific surface area through the implementation of closed windows in regular structures has been demonstrated to enhance radiation efficiency. It is possible to adapt this procedure for application to other geometrical structure, with the objective of increasing radiation output.
- A relation between local specific surface area in the direction of the main flow and radiation efficiency was identified, which allows the design of geometrical structures with random pore distribution and targeted radiation-optimised pore size distribution.

CRediT authorship contribution statement

Petra Weinbrecht: Writing – review & editing, Writing – original draft, Validation, Investigation, Data curation, Conceptualization. **Björn Stelzner:** Writing – review & editing, Methodology, Funding acquisition. **Peter Habisreuther:** Writing – review & editing, Methodology. **Christof Weis:** Writing – review & editing, Supervision. **Dimosthenis Trimis:** Supervision, Project administration, Funding acquisition.

Declaration of competing interest

The authors declare that they have no known competing financial interests or personal relationships that could have appeared to influence the work reported in this paper.

Data availability

Data will be made available on request.

Acknowledgements

This project has received funding from the European Union's Horizon 2020 research and innovation programme under grant agreement No. 768692

References

[1] Mathis WM, Ellzey JL. Flame stabilization, operating range, and emissions for a methane/air porous burner. Combust Sci Technol 2003;175(5):825–39. http://dx.doi.org/10.1080/00102200302411.
[2] Djordjevic N, Habisreuther P, Zarzalis N. Porous burner for application in stationary gas turbines: An experimental investigation of the flame stability, emissions and temperature boundary condition. Flow Turbul Combust 2012;89(2):261–74. http://dx.doi.org/10.1007/s10494-011-9381-9.
[3] Kaewchart K, Krittacom B. Comparison of combustion behavior between solid porous burners installed the porous emitter and non-porous emitter. Energy Procedia 2017;138:2–7.
[4] Kesting A, Pickenäcker K, Trimis D, Cerri I, Krieger R, Schneider H. Development of a highly efficient gas infrared heater by means of combustion in inert porous media. Int Gas Res Conf Proc 2001.
[5] Trimis D, Pickenäcker O, Wawrzinek K. Porous burners. Cell Ceram Struct Manuf Prop Appl 2005;484–508.
[6] Babkin V, Korzhavin A, Bunev V. Propagation of premixed gaseous explosion flames in porous media. Combust Flame 1991;87(2):182–90. http://dx.doi.org/10.1016/0010-2180(91)90168-B.
[7] Djordjevic N. flammenstabilisierung durch verbrennung infesten schwämmen [Ph.D. thesis], Karlsruhe: Karlsruher Institut für Technologie; 2011.
[8] Bedoya C. Stationary flames within porous inert media [Ph.D. thesis], Karlsruhe: Karlsruher Institut für Technologie; 2016.
[9] Dinkov I. Experimentelle und theoretische Untersuchungen zu der Verbrennung in radial-durchströmten porösen inerten Medien [Ph.D. thesis], Karlsruhe: Karlsruher Institut für Technologie; 2017.
[10] Wieland C, Weinbrecht P, Weis C, Habisreuhter P, Trimis D. Development of a porous burner for low calorific gaseous fuels offering a wide operating range. In: Proceedings of the European combustion meeting. 2019.
[11] AL-Hamamre Z, Diezinger S, Talukdar P, von Issendorff F, Trimis D. Combustion of low calorific gases from landfills and waste pyrolysis using porous medium burner technology. Process Saf Environ Prot 2006;84(4):297–308. http://dx.doi.org/10.1205/psep.05167.
[12] WU X-s, CHENG L-m, YAN K, ZHANG W-g. Experimental study of industrial low nitrogen porous media burner. J Zhejiang Univ Eng Sci 2018;52(11):2136–41.
[13] Al-attab KA, Ho JC, Zainal ZA. Experimental investigation of submerged flame in packed bed porous media burner fueled by low heating value producer gas. Exp Therm Fluid Sci 2015;62:1–8. http://dx.doi.org/10.1016/j.expthermflusci.2014.11.007.
[14] Huang R, Cheng L, Qiu K, Zheng C, Luo Z. Low-calorific gas combustion in a two-layer porous burner. Energy Fuels 2016. http://dx.doi.org/10.1021/acs.energyfuels.5b02399.
[15] Loukou A, Frenzel I, Klein J, Trimis D. Experimental study of hydrogen production and soot particulate matter emissions from methane rich-combustion in inert porous media. Int J Hydrog Energy 2012;37(21):16686–96. http://dx.doi.org/10.1016/j.ijhydene.2012.02.041.
[16] Zheng C, Cheng L, Saveliev A, Luo Z, Cen K. Gas and solid phase temperature measurements of porous media combustion. Proc Combust Inst 2011;33(2):3301–8.
[17] Gao H, Qu Z, Tao W, He Y, Zhou J. Experimental study of biogas combustion in a two-layer packed bed burner. Energy Fuels 2011;25(7):2887–95. http://dx.doi.org/10.1021/ef200500j.
[18] Khanna V, Goel R, Ellzey JL. Measurements of emissions and radiation for methane combustion within a porous medium burner. Combust Sci Technol 1994;99(1–3):133–42. http://dx.doi.org/10.1080/00102209408935429.
[19] Dai H, Lin B. Scale effect of ceramic foam burner on the combustion characteristics of low-concentration coal mine methane. Energy Fuels 2014;28(10):6644–54. http://dx.doi.org/10.1021/ef501349z.
[20] Caetano NR, Lorenzini G, Lhamby AR, Guillet VMM, Klunk MA, Rocha LAO, et al. Experimental assessment of thermal radiation behavior emitted by solid porous material. Int J Heat Technol 2020;38(1):1–8.
[21] Su S-S, Lai W-H, Hwang S-J. Experimental study of the heat recovery rate in a porous medium combustor under different hydrogen combustion modes. Int J Hydrog Energy 2016;41(33):15043–55.
[22] Yan C, Hao L, Hussein A, Raymont D. Evaluations of cellular lattice structures manufactured using selective laser melting. Int J Mach Tools Manuf 2012;62:32–8.
[23] Maznoy A, Kirdyashkin A, Minaev S, Markov A, Pichugin N, Yakovlev E. A study on the effects of porous structure on the environmental and radiative characteristics of cylindrical Ni-Al burners. Energy 2018;160:399–409.
[24] Fuessel A, Klemm H, Boettge D, Marschallek F, Adler J, Michaelis A. Advancement of cellular ceramics made of silicon carbide for burner applications. IOP Conf. Ser. Mater. Sci. Eng. 2011;18(18):182001. http://dx.doi.org/10.1088/1757-899X/18/18/182001.
[25] Pickenaecker O, Pickenaecker K, Heymer H, Tauscher W, Jansen F, Wawrzinek K, et al. Innovative ceramic materials for porous-medium burners. Interceram 1999.
[26] Gianella S, Gaia D, Ortona A. High temperature applications of Si-SiC cellular ceramics. Adv Energy Mater 2012. http://dx.doi.org/10.1002/adem.201200012.
[27] Rezaei E, Haussener S, Gianella S, Ortona A. Early-stage oxidation behavior at high temperatures of SiSiC cellular architectures in a porous burner. Ceram Int 2016;42(14):16255–61. http://dx.doi.org/10.1016/j.ceramint.2016.07.159.
[28] Colombo P. Conventional and novel processing methods for cellular ceramics. Phil Trans R Soc A 2006;364(1838):109–24.
[29] Ortona A, D'Angelo C, Gianella S, Gaia D. Cellular ceramics produced by rapid prototyping and replication. Mater Lett 2012;80:95–8. http://dx.doi.org/10.1016/j.matlet.2012.04.050, Cited by: 77.
[30] Pelanconi M, Bianchi G, Colombo P, Ortona A. Fabrication of dense SiSiC ceramics by a hybrid additive manufacturing process. J Am Ceram Soc 2022;105(2):786–93.
[31] Bianchi G, Gianella S, Ortona A. Design and additive manufacturing of periodic ceramic architectures. J Ceram Sci Technol 2017;8:59–66. http://dx.doi.org/10.4416/JCST2016-00088.
[32] Sobhani S, Muhunthan P, Boigné E, Mohaddes D, Ihme M. Experimental feasibility of tailored porous media burners enabled via additive manufacturing. Proc Combust Inst 2021;38(4):6713–22.
[33] Samoilenko M. Design of porous medium burners by means of additive manufacturing [Ph.D. thesis], Montreal: Department of mechanical engieering; 2018.
[34] Fleck NA. An overview of the mechanical properties of foams and periodic lattice materials. Cell Met Polym 2004;3–7.
[35] Elverum P, Ellzey J, Kovar D. Durability of YZA ceramic foams in a porous burner. J Mater Sci 2005;40(1):155–64.
[36] Wharton J, Ellzey J, Bogard D. An experimental study of turbulence intensities and non-uniformities in the exit flow from a porous combustor. Exp Fluids 2005;38(6):701–7.
[37] Neno RJ, Dias BS, Navalho JE, Pereira JC. Numerical simulation of heat removal from a window slab partition of a radiative coil coating oven. Energies 2022;15(6):2080.
[38] Stelzner B, Keramiotis C, Voss S, Founti MA, Trimis D. Analysis of the flame structure for lean methane–air combustion in porous inert media by resolving the hydroxyl radical. Proc Combust Inst 2015;35(3):3381–8. http://dx.doi.org/10.1016/j.proci.2014.06.151.
[39] Speyer RF, Lin W-Y, Agarwal G. Performance evaluation of porous radiant gas burners. Exp Heat Transf Int J 1995;8(1):73–95.
[40] Mital R. A study of the structure of submerged reaction zone in porous ceramic radiant burners. Combust Flame 1997;111(3):175–84. http://dx.doi.org/10.1016/S0010-2180(97)00006-0.
[41] Mital R, Gore J, Viskanta yR. A radiation efficiency measurement procedure for gas-fired radiant burners. Exp Heat Transf Int J 1998;11(1):3–21.
[42] Abdelaal M, El-Riedy M, El-Nahas A. Effect of oxygen enriched air on porous radiant burner performance and NO emissions. Exp Therm Fluid Sci 2013;45:163–8.
[43] Devi S, Sahoo N, Muthukumar P. Experimental studies on biogas combustion in a novel double layer inert Porous Radiant Burner. Renew Energy 2020;149:1040–52.
[44] Keramiotis C, Katoufa M, Vourliotakis G, Hatziapostolou A, Founti MA. Experimental investigation of a radiant porous burner performance with simulated natural gas, biogas and synthesis gas fuel blends. Fuel 2015;158:835–42. http://dx.doi.org/10.1016/j.fuel.2015.06.041.
[45] Vahidhosseini SM, Esfahani JA, Kim KC. Assessment of a cylindrical porous radiant burner with internal combustion regime for sustainable energy: Numerical analysis of the radiant efficiency and NO production. Sustain Energy Technol Assess 2021;43:100974.
[46] Wieland C, Weis C, Habisreuther P, Trimis D. 3D direct pore level simulations of radiant porous burners. Combust Flame 2022;245:112370.
[47] Diamantis D, Mastorakos E, Goussis D. Simulations of premixed combustion in porous media. Combust Theory Model 2002;6(3):383.
[48] Keramiotis C, Stelzner B, Trimis D, Founti M. Porous burners for low emission combustion: An experimental investigation. Energy 2012;45(1):213–9. http://dx.doi.org/10.1016/j.energy.2011.12.006.
[49] Inayat A, Freund H, Zeiser T, Schwieger W. Determining the specific surface area of ceramic foams: The tetrakaidecahedra model revisited. Chem Eng Sci 2011;66(6):1179–88.
[50] Antonia RA, Bilger RW. An experimental investigation of an axisymmetric jet in a co-flowing air stream. J Fluid Mech 1973;61(4):805–22. http://dx.doi.org/10.1017/S0022112073000959.

[51] Loukou A, Mendes M, Frenzel I, Pereira J, Ray S, Pereira J, et al. Experimental and numerical investigation of methane thermal partial oxidation in a small-scale porous media reformer. Int J Hydrog Energy 2017;42(1):652–63. http://dx.doi.org/10.1016/j.ijhydene.2016.11.062.
[52] Kiefer J, Weikl MC, Seeger T, von Issendorff F, Beyrau F, Leipertz A. Non-intrusive gas-phase temperature measurements inside a porous burner using dual-pump CARS. Proc Combust Inst 2009;32(2):3123–9. http://dx.doi.org/10.1016/j.proci.2008.06.026.
[53] Trimis D, Pickenäcker O, Wawrzinek K. Porous burners. Cell Ceram Struct Manuf Prop Appl 2005;484–508.
[54] Ortona A, Gianella S, Gaia D. SiC foams for high temperature applications. In: Advances in Bioceramics and Porous Ceramics IV: Ceramic Engineering and Science Proceedings. 32, Wiley Online Library; 2011, p. 153–61.
[55] Ortona A, Gaia D, Gianella S. High temperature applications of Si-SiC cellular ceramics. Adv Energy Mater 2012.
[56] Bianchi G, Di Mauro A, Ferrari L, Gianella S, Ortona A. Si-SiC oxidation barrier coating on 3D printed Si-SiC strut-based architectures deposited by electrophoretic deposition. J Eur Ceram Soc 2023;43(5):1790–6.
[57] Ortona A, Pusterla S, Fino P, Mach F, Delgado A, Biamino S. Aging of reticulated Si-SiC foams in porous burners. Adv Appl Ceram 2010;109(4):246–51.
[58] Bianchi G, Gianella S, Ortona A. Design and additive manufacturing of periodic ceramic architectures. J Ceram Sci Technol 2017;8(1):59–66.
[59] Fischedick T, Kind M, Dietrich B. Radial two-phase thermal conductivity of ceramic sponges up to high temperatures–experimental results and correlation. Int J Therm Sci 2017;114:98–113.
[60] Scheffler M, Colombo P. Cellular ceramics: Structure, manufacturing, properties and applications. John Wiley & Sons; 2006.
[61] Wu H, Chen Y-Y, Yang W, Xu X-C, Li B-W, LI Y. 3D Pore-Scale Numerical Investigation of Methane-Air Premixed Combustion in a Planar Radiant Porous Burner, Available at SSRN 4916856.
[62] Samoilenko M, Seers P, Terriault P, Brailovski V. Design, manufacture and testing of porous materials with ordered and random porosity: Application to porous medium burners. Appl Therm Eng 2019;158:113724.
[63] Habisreuther P, Djordjevic N, Zarzalis N. Statistical distribution of residence time and tortuosity of flow through open-cell foams. Chem Eng Sci 2009;64(23):4943–54.
[64] Grünbaum B, Shephard GC. Tilings with congruent tiles. Bull Amer Math Soc 1980;3(3):951–73.
[65] Loeb A. Space structures. Springer Science & Business Media; 2012.
[66] Pelanconi M, Rezaei E, Ortona A. Cellular ceramic architectures produced by hybrid additive manufacturing: A review on the evolution of their design. J Ceram Soc Japan 2020;128(9):595–604.
[67] Grosse J, Dietrich B, Martin H, Kind M, Vicente J, Hardy EH. Volume image analysis of ceramic sponges. Chem Eng Technol Ind Chem-Plant Equip-Process Eng-Biotechnol 2008;31(2):307–14.
[68] DIN. 15730 - Computed tomography in dimensional metrology - Measurement procedure and comparability. Beuth Verlag GmbH; 2019.
[69] Busch M, Hausotte T. Application of an edge detection algorithm for surface determination in industrial X-ray computed tomography. Prod Eng 2022;16. http://dx.doi.org/10.1007/s11740-021-01100-z.
[70] VDI. 2630, Blatt 1.4 - Computed tomography in dimensional metrology - Measurement procedure and comparability. Beuth Verlag GmbH; 2010.
[71] MATLAB. version 7.10.0 (R2018b). Natick, Massachusetts: The MathWorks Inc.; 2018.
[72] Derek Bradley, Gerhard Roth. Adaptive thresholding using the integral image. J Graph Tools 2007;12(2):13–21. http://dx.doi.org/10.1080/2151237X.2007.10129236.
[73] Gormley L. Image processing—continuous to discrete. Volume 1. Geometric, transform and statistical methods, by edward r. Dougherty and Charles R. Giardina. Int J Gen Syst 1987;13:363–4. http://dx.doi.org/10.1080/03081078708934986.
[74] Hansen CD, editor. The visualization handbook. [Online-ausg.]. Amsterdam: Elsevier-Butterworth Heinemann; 2005.
[75] DIN. EN 419 - Gas-fired overhead luminous radiant heaters for non-domestic use - Safety and energy efficiency. 2020.
[76] Modest MF. Radiative heat transfer. 2nd ed.. Amsterdam and Boston: Academic Press; 2003.
[77] Raab DH, Green EH. A cosine approximation to the normal distribution. Psychometrika 1961;26(4):447–50. http://dx.doi.org/10.1007/BF02289774.
[78] Warsza ZL, Korczynski MJ, Galovska M. Shifted UP cosine function as model of probability distribution. In: 19th IMEKO World Congress 2009, 4, January. 2009, p. 2308–13.
[79] Modest MF, Haworth DC. Radiative Heat Transfer in Turbulent Combustion Systems. Cham: Springer International Publishing; 2016, http://dx.doi.org/10.1007/978-3-319-27291-7.
[80] VDI E. VDI-Wärmeatlas. 10., bearb. und erw. Aufl. Aufl. Berlin: Springer; 2006.
[81] Garrido GI, Patcas F, Lang S, Kraushaar-Czarnetzki B. Mass transfer and pressure drop in ceramic foams: A description for different pore sizes and porosities. Chem Eng Sci 2008;63(21):5202–17.
[82] Devi S, Sahoo N. Impact of geometric parameters of fuel-air distribution system on the temperature variation and emission of a sideway faced porous radiant burner (SFPRB). In: Gas turbine India conference, Vol. 58509. American Society of Mechanical Engineers; 2017, p. V001T04A005.